Inference technique for the synaptic conductances in rhythmically active networks and application to respiratory central pattern generation circuits

Yaroslav I. Molkov[1], Anke Borgmann[2], Hidehiko Koizumi[2], Noriyuki Hama[2,3], Ruli Zhang[2], Jeffrey C. Smith[2]

[1]Department of Mathematics and Statistics, Neuroscience Institute, Georgia State University, Atlanta, GA

[2]Cellular and Systems Neurobiology Section, NINDS, NIH, Bethesda, MD

[3]Department of Neural and Muscular Physiology, Shimane University School of Medicine, Izumo City, Japan

Abstract

Unraveling synaptic interactions between excitatory and inhibitory interneurons within rhythmic neural circuits, such as central pattern generation (CPG) circuits for rhythmic motor behaviors, is critical for deciphering circuit interactions and functional architecture, which is a major problem for understanding how neural circuits operate. Here we present a general method for extracting and separating patterns of inhibitory and excitatory synaptic conductances at high temporal resolution from single neuronal intracellular recordings in rhythmically active networks. These post-synaptic conductances reflect the combined synaptic inputs from the key interacting neuronal populations and can reveal the functional connectome of the active circuits. To illustrate the applicability of our analytic technique, we employ our method to infer the synaptic conductance profiles in identified rhythmically active interneurons within key microcircuits of the mammalian (mature rat) brainstem respiratory CPG and provide a perspective on how our approach can resolve the functional interactions and circuit organization of these interneuron populations. We demonstrate the versatility of our approach, which can be applied to any other rhythmic circuits where conditions allow for neuronal intracellular recordings.

Introduction

Rhythmic neural circuits, which are ubiquitous in nervous systems (Buzsáki, 2006), generate spatiotemporal patterns of activity by synaptic interactions between neuronal populations, and unraveling the synaptic inputs to circuit neurons at high temporal resolution in the active networks is a major experimental problem in neurobiology for understanding circuit functional dynamics and architecture. Solving this problem ultimately requires electrophysiological methods to extract dynamic patterns of synaptic conductances in post-synaptic neurons from intracellular recordings during network activity. These patterns often involve temporally complex excitatory and inhibitory synaptic inputs, and thus methods to extract these inputs must be able to delineate the excitatory and inhibitory components, which can be superimposed during circuit activity, complicating the problem. This study presents a robust and versatile method to extract and separate inhibitory and excitatory synaptic conductance patterns from intracellular recordings. The technique is applicable to any periodically active network where the oscillation period significantly exceeds the interspike intervals of individual neurons. A synaptic conductance pattern refers to its temporal profile within a single network oscillation cycle. We designed our method to be compatible with various experimental setups, including current-clamp and voltage-clamp protocols, by focusing on the fundamental principles of electrophysiology and network dynamics. Our technique ensures high-resolution temporal profiling of synaptic inputs, making it adaptable to a wide range of rhythmically active neuronal circuits such as vertebrate and invertebrate motor pattern generation (CPG) networks (e.g., (Calabrese & Marder, 2024)), and cortical circuit rhythms (Yuste *et al.*, 2005). This generalizability highlights the potential of our approach to provide new insights into the functional organization and dynamics of diverse rhythmic neural circuits. Our approach extends previously proposed methods for extracting dynamic patterns of input synaptic conductances from intracellular recordings from neurons in a variety of circuits (Borg-Graham *et al.*, 1998; Anderson *et al.*, 2000; Shu *et al.*, 2003; Berg *et al.*, 2007; Endo & Kiehn, 2008; Wright & Calabrese, 2011) by providing nearly continuous, high-resolution readouts of excitatory and inhibitory synaptic conductances that are essential for deciphering circuit functional interactions.

To illustrate the utility of our technique, we applied this to circuits in the mammalian brainstem respiratory CPG, which is the fundamental rhythmic neural system that generates and controls breathing movements that are critical for homeostatic regulation of oxygen, carbon dioxide and pH in the brain and body (Feldman & Smith, 1995; Richter & Smith, 2014). These circuits are continuously active in various experimental preparations and the experimental accessibility of these circuits provides the opportunity

to apply our methods to investigate cellular and network electrophysiological processes underlying rhythmic motor pattern generation in a physiologically important mammalian system (Richter & Spyer, 2001; Smith *et al.*, 2013) . The rhythmic patterns of alternating inspiratory and expiratory phase neuronal activities that coordinate activity of spinal and cranial motoneurons during breathing originate within interacting pontine-medullary excitatory and inhibitory circuits in the brainstem (Cohen, 1979; Bianchi *et al.*, 1995; Feldman & Smith, 1995; Richter, 1996; Smith *et al.*, 2013). We have targeted specific respiratory microcircuits in the medulla of mature rat brainstem-spinal cord preparations *in situ* containing a variety of neuronal phenotypes and synaptic interactions that are key to the operation of the respiratory CPG. This allowed us to perform single neuron intracellular recordings from various neuronal types in different microcircuits, test different recording protocols to assess the robustness of our approach, and provides examples of how our technique can extract complex patterns of synaptic conductances at high temporal resolution in different types of rhythmic neurons. We illustrate how the synaptic conductance profiles throughout the respiratory cycle imply a "functional connectome" of respiratory circuit interactions, demonstrating the efficacy of our technique to provide novel information on circuit dynamic organization and operation.

Results

The general theoretical aspects of our approach for analyzing neuronal excitatory and inhibitory conductances from intracellular recordings in rhythmic circuits, and their specific application to the rhythmically active respiratory circuits, are delineated below. Our objective was to extract synaptic conductance dependence on the phase of the network activity cycle (hereinafter referred to as *synaptic conductance profiles*) representing nearly continuous readouts of excitatory and inhibitory synaptic inputs from the neuronal recordings throughout a cycle of periodic neural activity— the respiratory cycle in our illustration. Any periodic activity can be analyzed in the same way that we describe in this illustration below.

Reconstruction of synaptic inputs from intracellular recordings

The reconstruction of synaptic conductance profiles is based on the current balance equation:

$$C\frac{dV_m}{dt} = g_{leak}(E_{leak} - V_m(t)) + g_i(t)\big(E_i - V_m(t)\big) + g_e(t)\big(E_e - V_m(t)\big) + I_{inj}(t) \qquad (1)$$

where C is the membrane capacitance, V_m is the membrane potential, g_{leak} and E_{leak} are the conductance and the reversal potential of the leak current respectively, $g_i(t)$ and $g_e(t)$ are inhibitory and excitatory conductances (subject to retrieval), E_i and E_e are reversal potentials of inhibitory and excitatory synaptic currents, and $I_{inj}(t)$ is the injected current. We assume that the membrane potential of the cell is in instantaneous equilibrium ($dV_m/dt = 0$), which implies that the membrane time constant C/g_{leak} is much shorter than the time scale of the synaptic conductance variations. This assumption defines the time resolution of our method. For example, g_{leak}/C ratio in the respiratory interneurons was found to be in the range of 80 to 120 pS/pF (Koizumi & Smith, 2008) corresponding to the membrane time constant values of about 10 ms. Synaptic inputs originate from the periodically active network. The respiratory cycle period in our in-situ brainstem rat preparation typically spans approximately 2 seconds (***Figure 1***), yielding a time resolution of roughly 1/200 of the period. This approach to determining time resolution can be similarly applied to other systems.

Another important assumption is that Equation (1) does not include voltage-dependent currents. This means that the equation is simplified to only consider the passive properties of the membrane, such as resistance and capacitance. To ensure that voltage-dependent currents are minimized during the recording, a hyperpolarizing current injection protocol is employed. This involves injecting a negative current into the neuron, which drives the membrane potential to a more negative value. In our test recordings the membrane potential typically held between -100 and -60 mV. At this hyperpolarized state, most voltage-gated ion channels are closed, preventing the activation of voltage-dependent currents.

The phase of the respiratory cycle was defined as a piece-wise linear function of time in the following way: $\varphi(t) = (t - t_k)/(t_{k+1} - t_k)$, for times t between the time moments of two consecutive inspiratory phase onsets t_k and t_{k+1}. Our approach was based on the idea that in a network exhibiting periodic dynamics, the synaptic conductances depend on the cycle phase and not on time explicitly, so that $g_{i,e}(t) = g_{i,e}(\varphi(t))$. The respiratory cycle was divided into 100 bins of phase values, and for each bin the time moments $\{t_{ik}: \varphi(t_{ki}) \in [\varphi_i, \varphi_{i+1}]\}$ that correspond to phases in the bin were collected. For each phase bin i of the respiratory cycle, the relationship between the injected current $I_{inj}(t_{ik})$ and the membrane potential $V_m(t_{ik})$, where t_k are the times that correspond to the phase bin, appears fairly linear (see ***Figure 1B*** and ***Figure 1 Supplemental Figure 1***). Therefore, by linear regression we can find the slope and V-intercept of this dependence in the form:

$$V_m(t_k) = V_0(\varphi) + R(\varphi) \cdot I_{inj}(t_k) + \delta V_m(t_k) \qquad (2)$$

where $\varphi = (\varphi_i + \varphi_{i+1})/2$ is the center of the bin. The slope $R(\varphi)$ represents the total resistance, the intercept $V_0(\varphi)$ is the effective resting potential for the phase of the cycle φ, and $\delta V_m(t_k)$ are random fluctuations of the membrane voltage. Total conductance $G(\varphi)$ was calculated as the reciprocal of the total resistance, $G(\varphi) = 1/R(\varphi)$. The total conductance has static (phase-independent) and dynamic (phase-dependent) components. The latter is assumed to be a sum of dynamic components of the inhibitory and excitatory synaptic conductances. Synaptic conductances can also have static components whose combination cannot be distinguished from a static conductance of any other nature. Accordingly, we can think of the total conductance as a superposition of inhibitory and excitatory conductances whose static components form a static component of the total conductance, and their dynamic components underlie dynamic changes in the total conductance. Hence, the total current can be thought as a combination of the inhibitory and excitatory currents:

$$G(\varphi)(V_m - V_0(\varphi)) = G_i(\varphi)(V_m - E_i) + G_e(\varphi)(V_m - E_e), \tag{3}$$

where $G_i(\varphi)$ and $G_e(\varphi)$ are inhibitory and excitatory synaptic conductances, and E_i and E_e are corresponding reversal potentials. This equation must be fulfilled for any V_m, therefore

$$G(\varphi) = G_i(\varphi) + G_e(\varphi), \tag{4}$$

$$G(\varphi)V_0(\varphi) = G_i(\varphi)E_i + G_e(\varphi)E_e. \tag{5}$$

Solving this system of equations for the synaptic conductances yields

$$G_i(\varphi) = G(\varphi)(E_e - V_0(\varphi))/(E_e - E_i), \tag{6}$$

$$G_e(\varphi) = G(\varphi)(V_0(\varphi) - E_i)/(E_e - E_i). \tag{7}$$

To find the dynamic components of the synaptic conductances $\Delta G_i(\varphi)$ and $\Delta G_e(\varphi)$ we subtract their minimal values over the respiratory cycle:

$$\Delta G_i(\varphi) = G_i(\varphi) - \min_\varphi G_i(\varphi), \tag{8}$$

$$\Delta G_e(\varphi) = G_e(\varphi) - \min_\varphi G_e(\varphi). \tag{9}$$

Finally, we can use the sum of the minimal values found as an estimate for the leak conductance:

$$g_{leak} = \min_\varphi G_i(\varphi) + \min_\varphi G_e(\varphi). \tag{10}$$

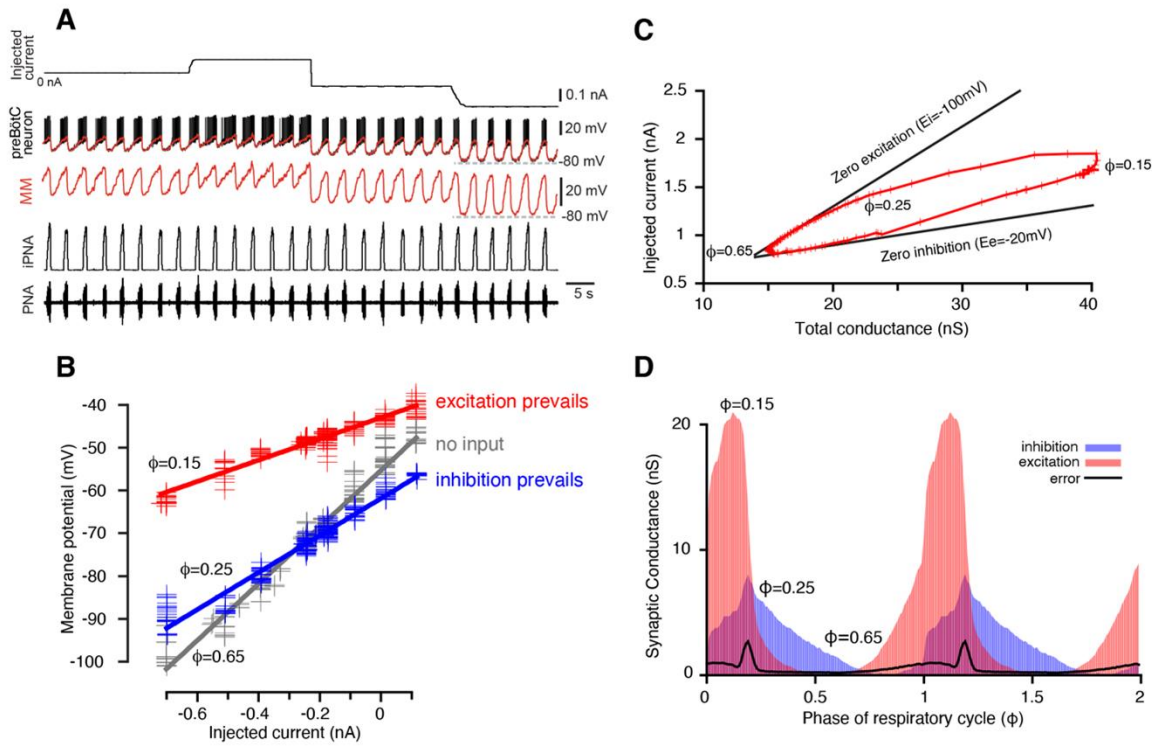

Figure 1. Reconstruction of synaptic conductance profiles. (**A**) An example of the intracellular recording from a rhythmic inspiratory neuron (2nd trace from top) during the stepwise current injection (top trace) protocol that we used for our analyses. Extracellular recording of phrenic nerve activity (PNA, bottom trace) and integrated PNA (iPNA, 4rd trace from top) are used for reference. The red trace shows a moving median (MM) filtration with a 0.1s window of the voltage at higher voltage resolution in the 3rd trace. The MM filters out the spikes while preserving slow voltage waves**.** (**B**) Plots of injected current vs. membrane potential of a preBötC inspiratory neuron corresponding to three selected values of the respiratory cycle phase (φ). Straight lines of the same colors show best linear fits. The parameters of the fits – the slope and *y*-intercept – are used to estimate the total resistance and the resting potential, respectively, for each phase of the cycle. (**C**) A typical example of the wedge diagram. Red plusses represent parameters of linear regressions for 100 phase values. The x-coordinate of each point is the total conductance $G(\varphi) = 1/R(\varphi)$, and the y-coordinate is $I_0(\varphi)$ (see Eqs. (2) and (11)). Thick black lines are zero excitation (upper boundary) and zero inhibition (lower boundary) lines, respectively (see Eqs. (13) and (14)). The slopes of the lines correspond to the reversal potentials for inhibition and excitation. (**D**) Calculated dynamic components of synaptic conductances from the same recording using

Eqs. (6-9) as functions of the phase of the respiratory cycle. Two cycles are shown with integer values of the phase (0, 1, 2) corresponding to a transition from expiration to inspiration. The excitatory synaptic conductance is shown in red, and the inhibitory conductance is shown in blue.

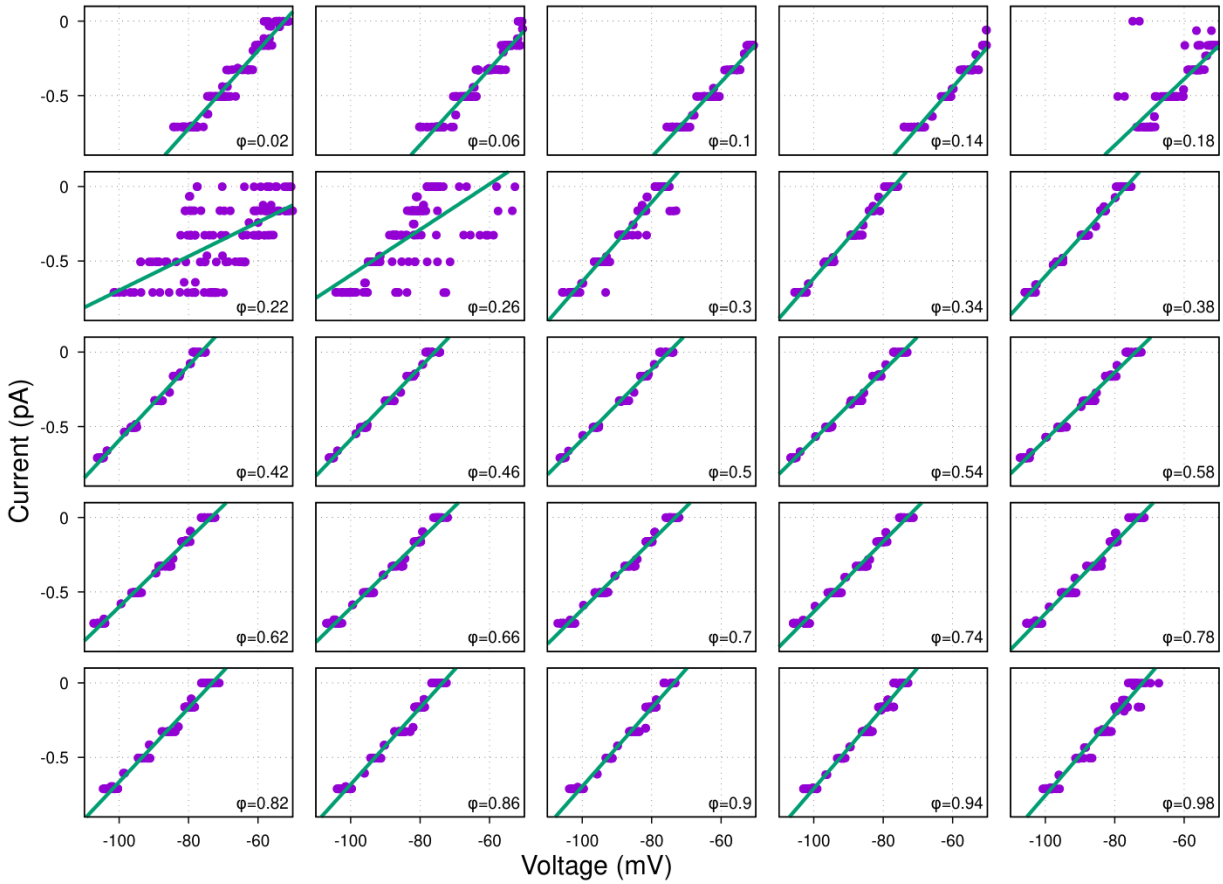

Figure 1 Supplemental Figure 1. Linear regressions of the injected current vs. membrane voltage for different phases of the respiratory cycle. Shown are the injected current (y-axis) vs. membrane voltage (x-axis) relations for 25 different phases of the respiratory cycle from a current-clamp recording from a ramp-I preBötC neuron. The phase value is indicated in the bottom right corner of each plot. This figure illustrates that the phase-specific current-voltage dependencies are almost perfectly linear in a wide range of voltage values. The exception is the interval of phase values near the transition from inspiration to expiration (0.2-0.25 for this particular recording) which reflects some cycle-to-cycle variability of the inspiratory phase durations. Less perfect linear fits near the transitions between respiratory phases manifest as bumps in the error estimates shown by black lines in ***Figures 1D, 3, 5, 6, 7***.

Reversal potential estimation

It is possible that during a certain part of the cycle, a neuron receives only one type of synaptic input, inhibitory or excitatory. Below is how this fact can be exploited for obtaining the estimates of reversal potentials for inhibition or excitation. For inhibition, after introducing

$$I_0(\varphi) = -G(\varphi)V_0(\varphi) \tag{11}$$

in (5) and combining (4) and (5) we get:

$$I_0(\varphi) = -E_i G(\varphi) - G_e(\varphi)(E_e - E_i). \tag{12}$$

Since the total excitatory synaptic conductance $G_e(\varphi)$ is greater or equal to its static component $G_e^0 = \min_\varphi G_e(\varphi)$, from (12) it follows that a straight line on the (G, I_0)-plane described by

$$I_0(\varphi) = -E_i G(\varphi) - G_e^0(E_e - E_i) \tag{13}$$

serves as an upper boundary of the reconstructed trajectory $\{(G(\varphi), I_0(\varphi)), \varphi \in [0,1]\}$. If we suppose that the neuron receives only phase-dependent inhibition in a certain range of phase, i.e., the excitatory synaptic conductance is equal to its static component in this range, $G_e(\varphi) = G_e^0$, then the trajectory moves strictly along the line described by (13) which can be referred to as a *zero excitation line*. By identifying the upper portion of the trajectory with nearly linear behavior we can perform linear regression of this portion to find its slope $-E_i$, and thus estimate the reversal potential for inhibition (see ***Figure 1C***). Similarly, for the phases of the cycle where only excitatory input is present, we can derive:

$$I_0(\varphi) = -E_e G(\varphi) + G_i^0(E_e - E_i) \tag{14}$$

where $G_i^0 = \min_\varphi G_i(\varphi)$ is a static component of the inhibitory conductance and call it the *zero inhibition line*. The latter obviously serves as a lower boundary of the trajectory. Together the zero excitation and zero inhibition lines form a wedge that bounds the trajectory, so hereinafter we refer to such plots as *wedge diagrams* (***Figure 1C***).

Interestingly, the linear upper boundary of the trajectory was seen in almost all recordings processed implying that, first, during certain phase(s) of the respiratory cycle the interneurons indeed receive only inhibitory input, and second, we could use the identified parameters of the zero-excitation line to measure the inhibitory reversal potential. The same approach might be applied for the

determination of the reversal potential for excitation if there was a certain range of phases when a cell received the excitatory input only. Since E_e is expected to be close to 0 mV, this would be clearly identifiable by the presence of a nearly horizontal part of the curve serving as a lower boundary of the same. This kind of behavior was not found in most of the recordings, so, as commonly accepted, E_e was set to -10 mV in those cases. However, as we demonstrate below, variation of reversal potentials over a wide range of possible values does not affect the shape of synaptic conductance profiles qualitatively.

Firing patterns, synaptic input conductances, and inferred functional connectome of respiratory interneurons: an illustration

For our illustration of extracting synaptic conductances with the above approach, we targeted neurons in key interacting respiratory circuits located in discrete bilateral regions of the ventrolateral medulla, specifically in the preBötzinger complex (preBötC) region, which contains local excitatory and inhibitory circuit neurons critical for generating rhythmic inspiratory activity, and the adjacent more rostral Bötzinger complex (BötC) region (refer to ***Figure 2 Supplemental Figure 1***), containing neurons generating rhythmic expiratory activity that interact with preBötC circuits, including by inhibitory circuit connections (e.g., (Lindsey *et al.*, 2012; Smith *et al.*, 2013; Molkov *et al.*, 2017; Ausborn *et al.*, 2018). Thus, targeting these regional microcircuits allowed us to test our methods for extracting various patterns of excitatory and inhibitory synaptic inputs in two functionally distinct microcircuits. Also, there are various electrophysiological phenotypes of respiratory neurons with different patterns of neuronal spiking activity during the respiratory cycle in these regions, thus providing a diversity of rhythmic neuronal types to correlate with synaptic input patterns from our analysis, which is useful for illustrating the utility of our techniques for delineating various functional synaptic interactions. We have used sharp microelectrode intracellular recordings in mature rat brainstem-spinal cord preparations *in situ* (see Materials and methods) for our analysis since this approach allowed us to readily record deep in the brainstem in these targeted regions from multiple neurons under current- and voltage-clamp with a single electrode. This provides complementary information to test the robustness of our approach, which should be insensitive to the mode of intracellular recording. Although our techniques can be applied to any type of rhythmic neuron, we specifically targeted and analyzed interneurons, verified by immunochemistry (as described below and in Material and methods), which are the most technically challenging to record from due to small neuronal sizes and potential recording instability, but are functionally critical for analyzing synaptic mechanisms of neural activity pattern generation. Thus, we

231 could test how our technique performs for important neuronal populations under recording conditions
232 that would likely be encountered for many rhythmic interneuronal circuits in nervous systems.

233 ***Firing patterns of respiratory interneurons*.** Under normal physiological conditions the neuronal activity
234 during the respiratory cycle consists of three main activity phases [inspiratory (I), post-inspiratory (post-
235 I), and stage 2 or late expiratory (E2)] that are well documented in the literature (e.g., (Lindsey *et al.*,
236 2012; Richter & Smith, 2014). Previously described respiratory populations based on their specific firing
237 patterns in relation to these different phases of the cycle (see ***Figure 2***) include pre-
238 inspiratory/inspiratory (pre-I/I), ramping inspiratory (ramp-I), early-inspiratory (early-I), late inspiratory
239 (late-I), post-inspiratory (post-I) and augmenting expiratory (aug-E, active during E2) neurons. We have
240 recorded neurons from all these populations (***Figure 2***) and have analyzed and presented representative
241 synaptic input patterns (***Figure 3***) for each electrophysiological phenotype. In some cases, as an
242 informative addition to our electrophysiological analyses, we labeled the recorded neurons by
243 intracellular injection of biocytin contained in the electrode recording solution (see Materials and
244 methods) for subsequent histological verification (***Figure 2 Supplemental Figure 1***) of the recording
245 location, interneuron identification, and in some cases neurotransmitter phenotype by
246 immunohistochemistry (n=34 neurons total labeled). The latter enabled us to identify inhibitory neurons
247 (glycinergic or GABAergic) (e.g., see ***Figure 2 Supplemental Figure 2***) for five of the neuron types (pre-I/I,
248 ramp-I, early-I, post-I, aug-E) as described below, which aids in circuit analysis and the corroboration of
249 inhibitory inputs from neurons with particular firing patterns.

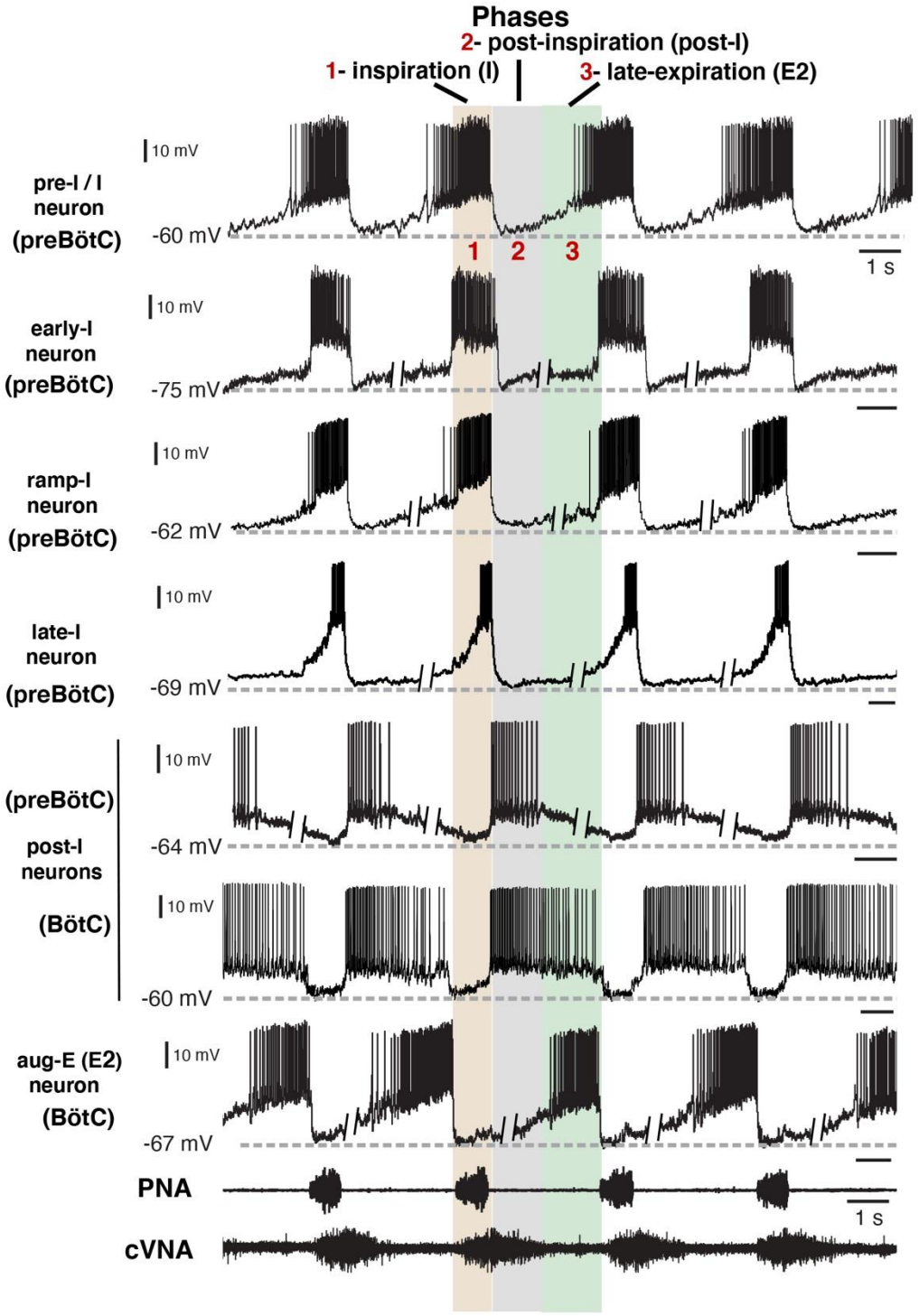

Figure 2. Firing patterns of respiratory interneurons. The traces are current clamp intracellular recordings from different types of respiratory neurons distinguished by their action potential firing patterns and activity during different respiratory cycle phases [inspiratory (I), post-I, or late-expiratory/E2 phase]. Extracellular recordings of the phrenic nerve activity (PNA) and central vagus nerve activity

255 (cVNA) are shown below as reference. The nerve recordings were obtained simultaneously with the pre-
256 I/I neuron recording. All other neuron recordings were obtained from different experimental
257 preparations and were composited and aligned according to phases of the cycle as indicated at the top.
258 This was done by deleting segments (as indicated) of the membrane potentials during the expiratory
259 phases, since the expiratory intervals largely determine the discharge frequencies which are variable
260 between the *in situ* preparations, while the inspiratory phase durations are very similar. All neurons
261 included in our study exhibited rhythmic firing patterns consistent with the three-phase organization of
262 the cycle and can be arranged in this format for purposes of illustration. Regions of the ventrolateral
263 medulla (preBötC or BötC) where these example recordings were obtained, as verified histologically
264 *(**Figure 2 Supplemental Figure 1**)*, are indicated.

265

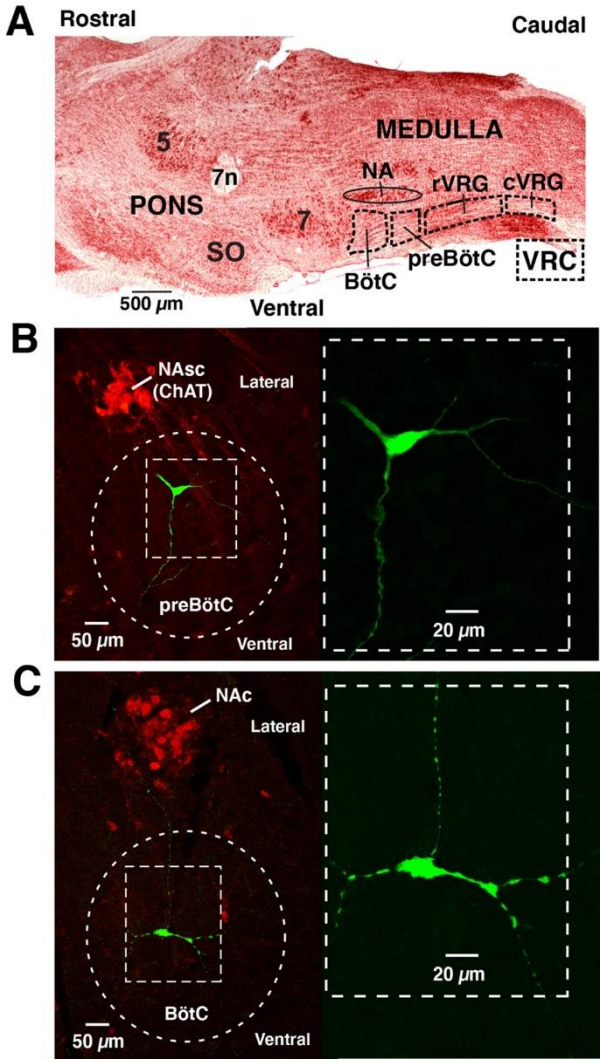

Figure 2 Supplemental Figure 1. **Respiratory regions of the brainstem ventrolateral medulla and intracellular recording sites. A**. Parasagittal view (neutral red stain) of the lateral medulla indicating regions of the ventral respiratory column (VRC) and locations of the preBötC and BötC regions of the VRC in the ventrolateral medulla, ventral to nucleus ambiguus (NA) that were targeted for intracellular recordings. Abbreviations: rVRG and cVRG, rostral and caudal ventral respiratory groups which also contain neurons of the respiratory CPG; 5 and 7, trigeminal and facial motor nuclei; 7n, facial nerve; SO, superior olivary nuclei. **B**. Example of histological reconstruction (confocal fluorescence images) of recorded inspiratory neuron (ramp-I) in the preBötC region ventral to motoneurons of NAsc (semi-compact division) labeled by immunostaining (red) for choline acetyltransferase (ChAT). The locations of rhythmic neurons used for our analyses were routinely verified by filling the cells with neurobiotin

286 by iontophoresis at the end of recording and fluorescently stained (see Methods), and in some cases
287 further processed for immuno-identification of neurotransmitter phenotype (see ***Figure 2 Supplemental***
288 ***Figure 2***). The immunostaining for ChAT was used as a landmark for regional recording locations, and
289 also to verify that recordings were obtained from interneurons and not motoneurons. A higher
290 magnification image of neuronal morphology with background removed is shown in the dashed box at
291 right. **C**. Example of histological reconstruction (confocal images) of a recorded expiratory neuron (aug-E)
292 and fluorescently stained in the BötC region ventral to motoneurons of NAc (compact division) labeled
293 by immunostaining (red) for ChAT. Higher magnification image of labeled neuron (background removed)
294 is shown at right.

295

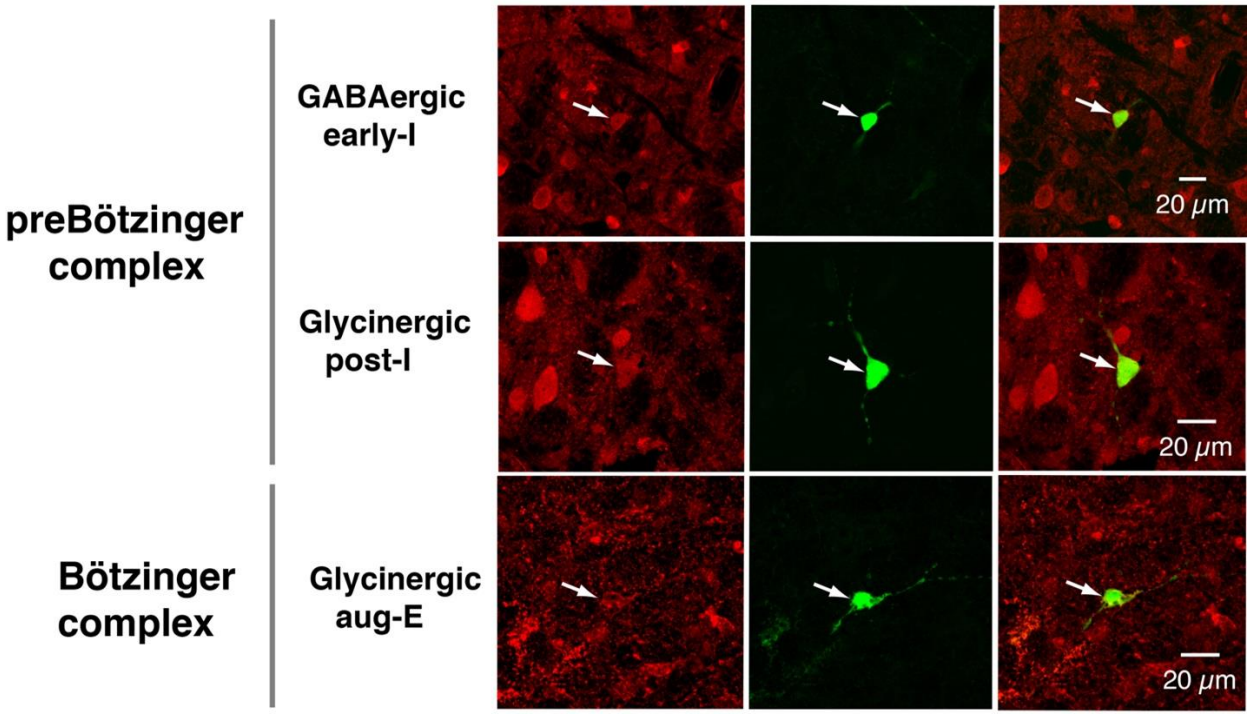

296

297 **Figure 2 Supplemental Figure 2. Identification of glycinergic or GABAergic inhibitory neurons**. Examples
298 from separate experiments of neurons filled with neurobiotin during the somatic intracellular recordings,
299 and subsequent immunohistochemistry with antibodies for glycine or GABA (red fluorescence), and
300 Alexa Fluor 488-Avidin D conjugate to label neurobiotin. Images shown for the labeled respiratory
301 neuron types in the ventrolateral medullary regions indicated are fluorescence single-plane confocal
302 images for the glycine or GABA antibody labeling (left panels), neurobiotin labeling (middle), and

303 superposition images showing double labeling (right). The single imaging planes shown were chosen to
304 optimize visualization of co-labeling of the somata of the recorded neuron in each case.

305

306 ***Synaptic conductances and functional connectome of respiratory interneurons. Figure 3*** shows the
307 synaptic conductance profiles of the major interneuronal electrophysiological phenotypes whose firing
308 patterns are illustrated in ***Figure 2***. Within one population of the same electrophysiological phenotype,
309 patterns of synaptic inputs were qualitatively similar, although there was neuron-to-neuron variability in
310 calculated conductance values and details of the conductance profiles could vary (***Figure 3***) among
311 multiple examples of each type of recorded neurons. From these temporal patterns of synaptic
312 conductances, as explained below we infer functional connectomes or circuit motifs for each
313 electrophysiological phenotype as illustrated in ***Figure 4***, which is an important outcome of our analyses.
314 In general, these circuit connections motifs are constructed by considering that the different
315 components of the synaptic conductance profiles are formed by convergent inputs from neuronal
316 populations of specific firing phenotypes and, therefore, can be interpreted as reflecting activity patterns
317 of these pre-synaptic populations. By matching these activity patterns with patterns of synaptic
318 conductances in the recorded post-synaptic neurons, we can suggest functional connections between
319 neuronal populations. The information on inhibitory transmitter phenotype for neurons with different
320 firing patterns was also collected and indeed corroborates that subsets of the presynaptic neurons are
321 inhibitory as inferred from the conductance profiles, which gives additional confidence in the correlation
322 between pre-synaptic firing patterns and likely post-synaptic interactions.

323

324

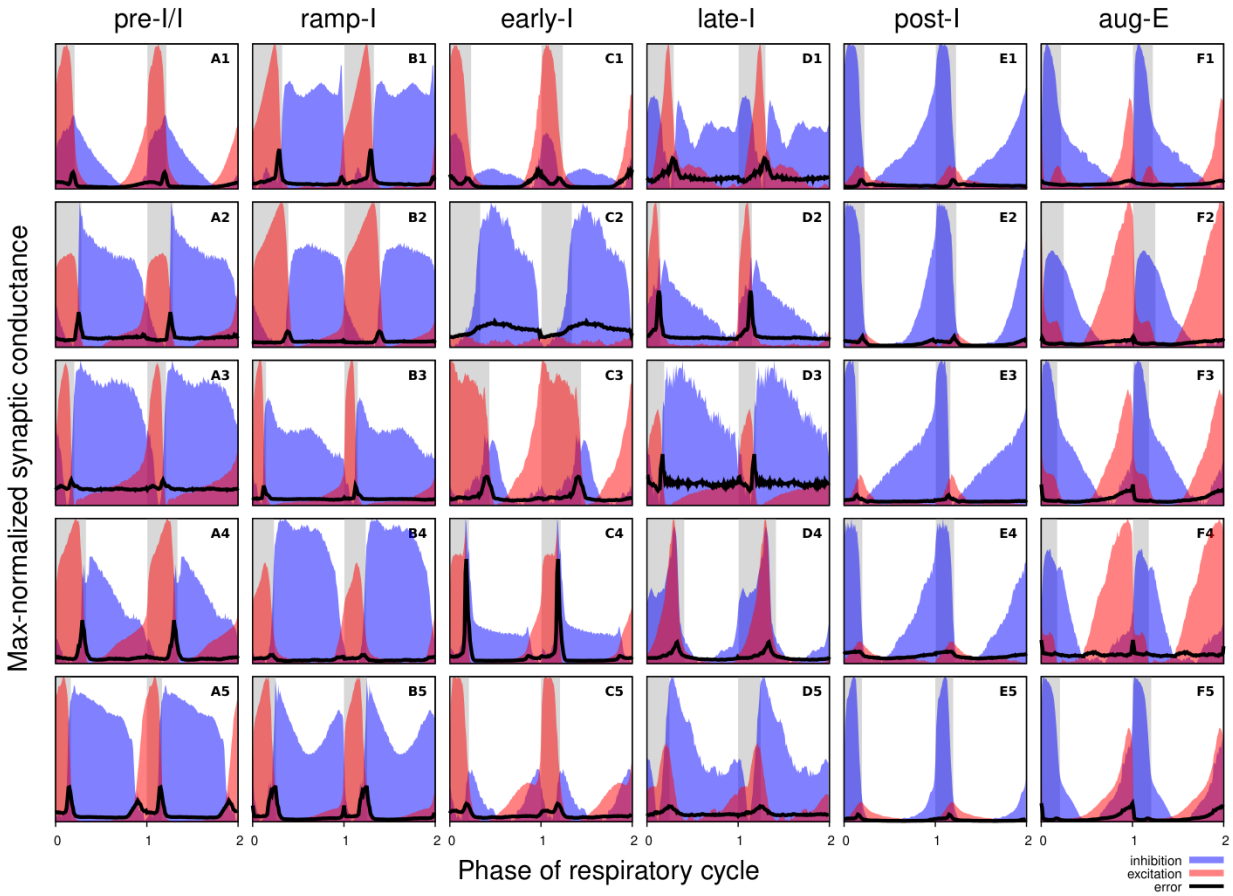

Figure 3. Synaptic conductance profiles of major respiratory neuronal phenotypes. Each panel depicts how the dynamic components of excitatory (red) and inhibitory (blue) synaptic conductances, normalized to the maximal value, vary with the cycle phase for an individual neuron. Neuronal firing phenotypes are listed on the top. Two respiratory cycles are shown so that transitions between the respiratory phases are clearly seen. The inspiratory phases are highlighted by grey bars. Integer phase values (0, 1, 2) correspond to transitions from expiration to inspiration as determined by onset of the phrenic motor output recorded simultaneously. The error for each phase value is indicated by a thick black line in each panel. Each panel is labelled according to the firing pattern of the recorded neuron (A: pre-I/I, B: ramp-I, C: early-I, D: late-I, E: post-I, F: aug-E).

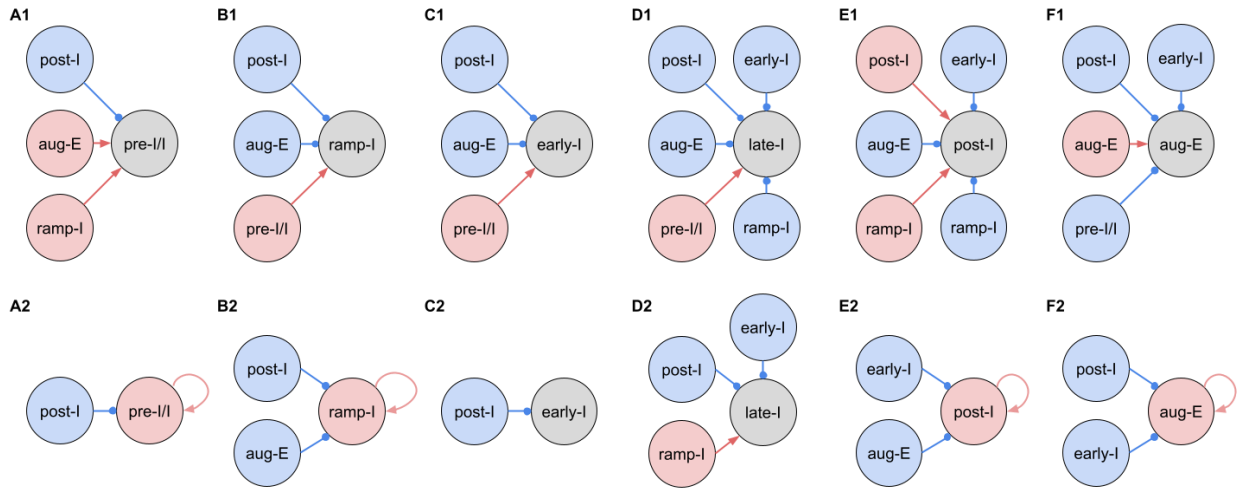

Figure 4. Inferred connections between different respiratory interneuronal populations. By matching the firing phenotype of the receiver neuron and its synaptic inputs we infer possible motifs of interactions between the functional populations of the active network. In this representation, we assume that the functional connection between populations is present, if a post-synaptic neuron of a particular firing phenotype has a dynamic component of the synaptic conductance statistically significantly different from zero (see Materials and methods: Statistical significance) in the phase range corresponding to the activity pattern of the pre-synaptic population. Here we show two examples of such inferences for each phenotype representing the most straightforward interpretation of synaptic inputs (***A1, B1, C1, D1, E1 and F1***) as well as interactions involving the least number of populations (***A2, B2, C2, D2, E2 and F2***), reflecting the cell-to-cell variability in conductance profiles with some neurons within a given electrophysiological phenotype exhibiting the smaller set of synaptic inputs. Possible inhibitory/excitatory connections are shown by blue/red lines ending with blue circles/red arrows originating from presynaptic neurons and terminating at the post-synaptic neurons. Inhibitory sources are shown in blue, and the excitatory sources are shown in red. These circuit motifs are consistent with the patterns of synaptic inputs to the various neurons, as described in the text for each electrophysiological phenotype, and account for our immuno-histochemical identification of inhibitory neurons as subpopulations of most of the electrophysiological types as indicated in the text.

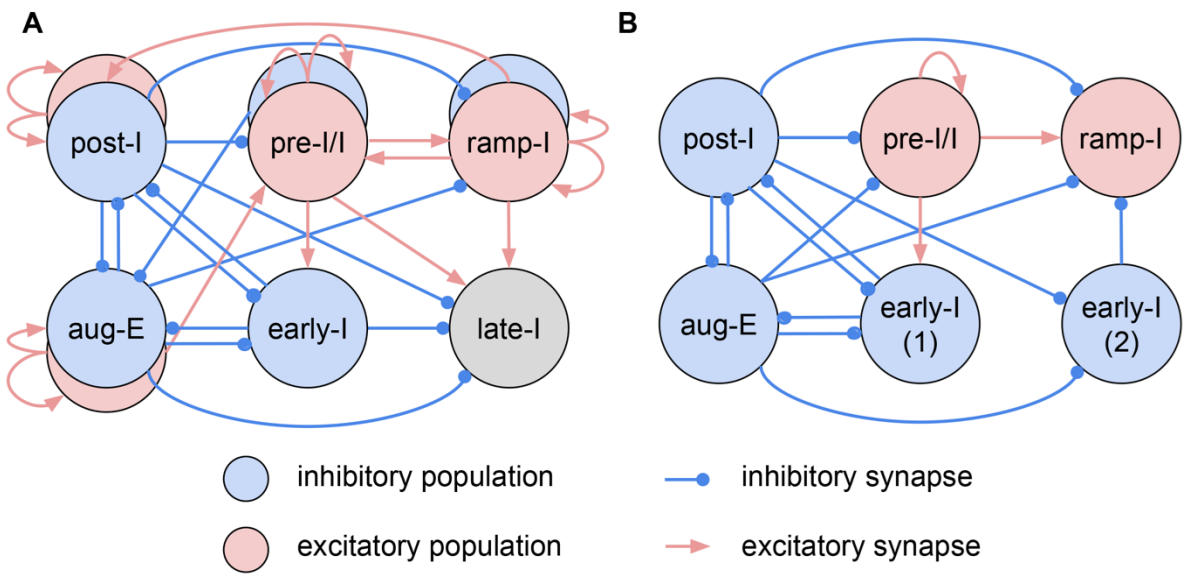

Figure 4 Supplemental Figure 1. Combinatorial circuit schematic. **A.** Comprehensive summary of the inferred connectome of the functional respiratory network, implied by the collection of circuit motifs shown in ***Figure 4***, incorporating information about proposed synaptic inputs and neurotransmission between various neuronal populations classified according to their distinct firing pattern phenotypes. This schematic incorporates all of the possibilities inferred from our conductance analyses, and includes sets of mutual inhibitory interactions between inhibitory populations (post-I and aug-E; early-I and post-I, early- I and aug-E populations), inhibitory inputs to excitatory populations (post-I to pre-I/I and ramp-I; aug-E to ramp-I), and the pre-I/I and ramp-I excitatory synaptic drives. **B.** A functionally minimal circuit schematic previously suggested by Smith *et al*. (2007) and shown from model simulation studies to generate a realistic three-phase rhythmic pattern of neuronal population activity. Similarities of the circuit interactions depicted in these two schematics include the inhibitory connectome with post-I and aug-E inhibition distributed throughout the network, the sets of mutual inhibitory interactions, and the strong pre-I/I excitatory inspiratory drive, while there are clearly additional features in our more elaborate circuit connectome in the new combinatorial schematic (**A**), including the inhibitory and excitatory neuronal counterparts and associated circuit interactions for post-I, aug-E, pre-I/I, and ramp-I neuron populations that were not included in the previous models. This connectivity suggests the idea that the excitatory subpopulations could drive the activity during their respective cycle phases and could synchronize activity of their inhibitory counterparts, whereas the inhibitory subpopulations appear to be important participants in orchestrating phase transitions and maintaining inhibition to other circuit populations during the active phases driven by the excitatory subpopulations.

375 To illustrate in more detail how we have reconstructed the circuit connection motifs in ***Figure 4***,
376 we describe how we interpret and translate the synaptic conductance profiles for each
377 electrophysiological phenotype.

378 Pre-I/I cells (n=25 neurons recorded in the preBötC) in all cases received decrementing
379 expiratory inhibition, and augmenting excitation during late expiration as well as strong ramping
380 inspiratory excitation (***Figure 3A1-5***). As shown In ***Figure 4A1***, a straight-forward interpretation of this
381 pattern of conductances is that the pre-I/I population receives inhibitory inputs from post-I spiking
382 neurons and excitatory inputs from aug-E and ramp-I populations. Alternatively, since a combination of
383 aug-E and ramp-I excitatory inputs is qualitatively similar to an input from the pre-I/I population itself, it
384 is also possible that excitatory pre-I/I neurons are recurrently interconnected within this population
385 (***Figure 4A2***). These possibilities are not mutually exclusive, and both connectivity patterns could be
386 expressed in the respiratory circuits. We labeled 13 of these pre-I/I neurons during recording, two of
387 which were identified as inhibitory neurons by neurotransmitter immuno-labeling for glycine or GABA (1
388 glycinergic and 1 GABAergic neuron identified), which is incorporated in ***Figure 4F1***.

389 Neurons with the ramp-I spiking patterns (n=24 recorded in preBötC) also received ramping
390 inspiratory phase excitation, but unlike some pre-I/I cells, they generally showed strong synaptic
391 inhibition throughout the post-inspiratory and late-expiratory (E2) phases (***Figure 3B1-5***). Some of these
392 neurons also received excitatory input during the E2 expiratory/pre-inspiratory phase. Therefore, it is
393 reasonable to suggest that ramp-I neurons receive inhibitory inputs from post-I and aug-E populations as
394 well as an excitatory input from pre-I/I neurons (***Figure 4B1***). Another possibility is that the excitatory
395 ramp-I neurons not receiving excitation during the pre-inspiratory phase have recurrent excitation within
396 their population (***Figure 4B2***). Four out of 7 of these neurons were labeled in the preBötC and identified
397 as inhibitory (glycinergic) neurons (incorporated in ***Figures 4D1&4E1*)*.***

398 All early-I spiking neurons (n=6 in preBötC) showed decrementing expiratory phase inhibition
399 (***Figure 3C1-5***). Most of these cells also received pre-inspiratory/late expiratory and inspiratory excitation
400 (***Figure 3C1, 3-5***), while some of them did not (***Figure 3C2***), which we interpret as shown in **Figures 4C1**
401 **and 4C2**, respectively. The excitatory pre-I/I input can also be a combination of aug-E and ramp-I
402 excitation as in ***Figure 4A1***. One of the three labeled early-I neurons was identified as an inhibitory
403 (GABAergic) neuron (***Figure2 Supplemental Figure 2***), corroborating the early-I inhibitory inputs inferred
404 from conductance profiles shown in ***Figures 4 D1&2, 4E1&E2, 4F1&F2***.

405 Synaptic inputs to late-I cells (n=6 in preBötC) were similar to ramp-I neurons (***Figure 3D1-5***) plus
406 concurrent, inspiratory phase inhibition. So, in addition to inhibitory inputs from post-I and aug-E
407 neurons and pre-I/I (in some cases) and ramp-I excitation, they likely receive inhibitory inputs from early-
408 I spiking neurons (***Figure 4D1***). Some of these cells showed neither inhibition nor excitation at the end of
409 expiration (***Figure 3D2***), so they might receive no aug-E inhibition and ramp-I rather than pre-I/I
410 excitation (***Figure 4D2***). These neurons were infrequently recorded, and none were successfully labeled
411 for neurotransmitter type identification.

412 Post-I spiking neurons (n=40: 25 in preBötC, 15 in BötC), that always exhibit a decrementing
413 firing pattern during expiration, received strong decrementing inhibition during inspiration, and
414 incrementing inhibition during late expiration (***Figure 3E1-5***). They also showed a relatively weak
415 excitation during post-inspiration, usually accompanied by comparable in magnitude ramping excitation
416 during inspiration. The corresponding circuit elements representing inputs to the post-I neurons are
417 shown in ***Figure 4E1***. Since post-I neurons receive post-I excitation, it is possible that excitatory post-I
418 cells form a population with recurrent excitatory interconnections. Besides, some of these neurons did
419 not have any significant excitatory input during inspiration (***Figure 3E3***). The latter possibilities are shown
420 in ***Figure 4E2***. Eight of the 20 post-I neurons labeled (5 in preBötC and 3 BötC neurons) were identified as
421 glycinergic (***Figure 2 Supplemental Figure 2***), consistent with a previous study (Ezure *et al.*, 2003), and
422 corroborating the post-I inhibitory inputs shown in ***Figures 4A1&2, 4B1&2, 4C1&2, 4D1&2, 4F1&2***.

423 Finally, all the aug-E spiking neurons (n=19 recorded: 9 neurons in preBötC, 10 in BötC) received
424 decrementing inhibitory inputs during expiratory and inspiratory phases as well as an excitatory input
425 that started in the middle of expiration and incremented towards the end of expiration (***Figure 3F1-5***).
426 Some of these neurons received pre-inspiratory inhibition. We interpret this as the aug-E population
427 receiving inputs from early-I, post-I and pre-I/I inhibitory populations and the excitatory input from aug-E
428 neurons (***Figure 4F1***). Similar to other interpretations, it is also possible that the excitatory aug-E
429 neurons form a population with recurrent excitation with an augmenting pattern that matches their
430 activity profile, while some of these neurons do not receive pre-I inhibition (***Figure 4F2***). Three out of 6
431 of these neurons labeled were identified as glycinergic neurons (1 preBötC neuron and 2 BötC neurons)
432 (***Figure 2 Supplemental Figure 2***), as inferred from the synaptic conductance profiles in ***Figures 4B1&2,***
433 ***4C1, 4D1, 4E1.***

434

435 **Validating reliability of inferred synaptic conductance profiles**

436 ***Synaptic conductance profiles from current- and voltage-clamp recordings.*** The traditional way to
437 measure transmembrane currents is by voltage-clamp intracellular recordings. Using this experimental
438 protocol, the membrane potential of the neuron is held at a constant level thus maintaining all voltage-
439 dependent membrane currents at their steady states. Therefore, in voltage-clamp conditions any total
440 current variations result exclusively from time-varying synaptic inputs, while in the current-clamp
441 protocol variations of the voltage can potentially be contaminated by transient dynamics of the voltage-
442 gated channels. However, the implementation of the voltage-clamp protocol is technically far more
443 challenging with sharp high-impedance microelectrodes than injecting a constant current. By design, our
444 technique is indifferent to what strategy is used for the injected current variations, so we performed
445 both current- and voltage-clamp recordings from select neurons (n=10) where the voltage-clamp could
446 be satisfactorily established following the current-clamp recording in each of these neurons and
447 compared the results of the synaptic input interferences as a test of the reliability of our methods.

448 ***Figure 5*** shows the excitatory and inhibitory synaptic conductance profiles extracted from
449 current- (left) and voltage-clamp (right) segments of the intracellular recordings for 3 different types of
450 representative neurons. It is evident that the shapes of the conductance profiles as well as the
451 relationship between the excitatory and inhibitory conductances extracted are very similar. Quantitative
452 variations in the amplitude of the synaptic inputs are similar to those observed when using different
453 epochs of the same current-clamp recordings (see below). Thus, we conclude that our synaptic
454 conductance inferences obtained by current clamp recordings favorably match the conductance profiles
455 obtained from direct recordings of synaptic currents during voltage clamp.

456

457

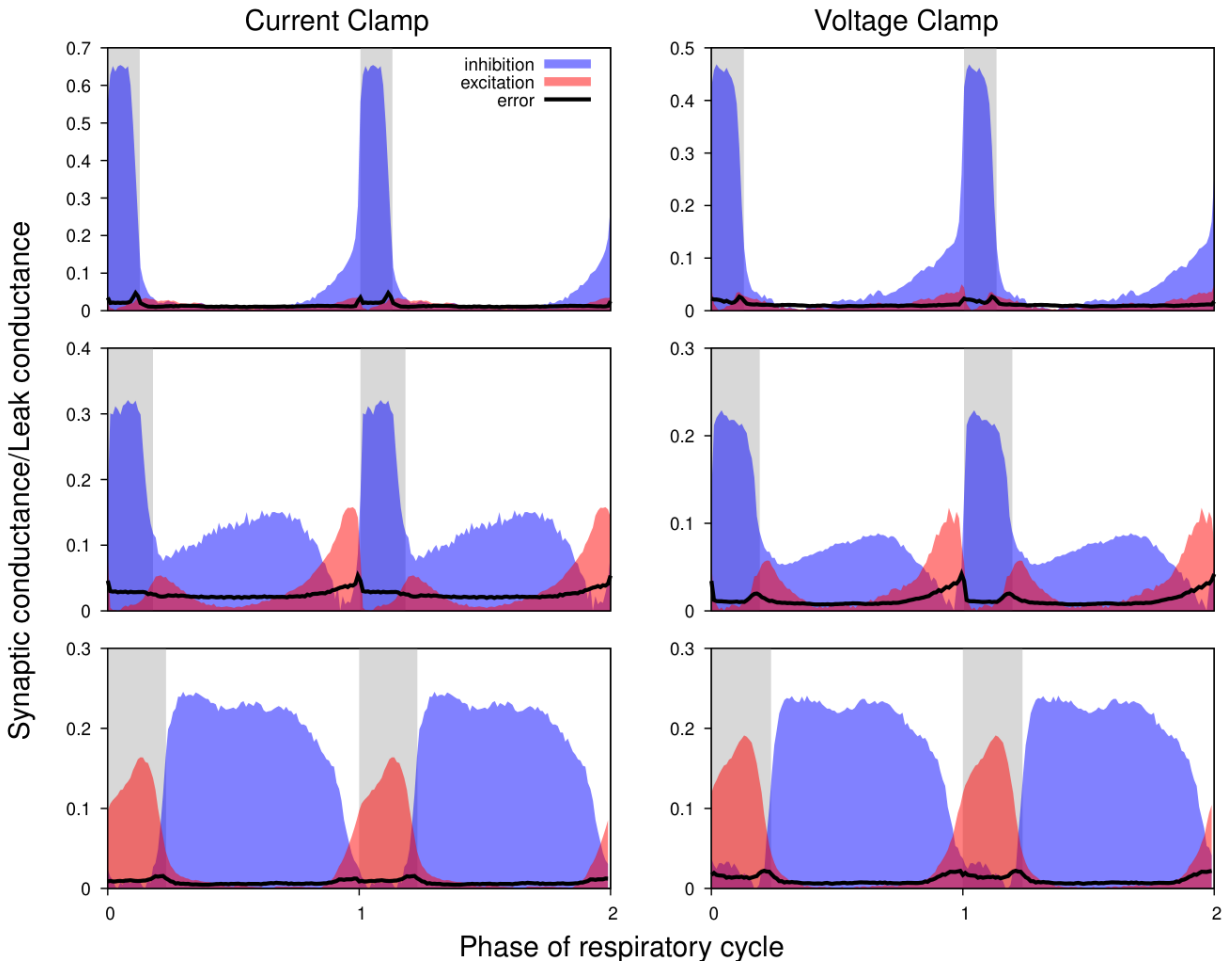

Figure 5. Comparison of the synaptic conductance profiles reconstructed from current- and voltage-clamp recordings. Conductance profiles for three representative preBötC neurons are illustrated (from current-clamp recordings at left and voltage-clamp recordings from the same neurons at right). Two respiratory cycles are shown for each neuron (post-I, top; aug-E, middle; ramp-I, bottom panels) with inspiratory phases highlighted by gray bars. Calculated synaptic conductances are normalized by the estimates of the leak conductance. While the absolute conductance values may vary, the shapes of the synaptic conductance profiles as well as the relationship between the excitatory and inhibitory conductances are consistent across these recording protocols.

469 ***Uncertainties concerned with estimates of synaptic reversal potentials***. As noted, it was not always
470 possible to identify linear portions of GI-contours suitable for reliable estimation of the reversal
471 potentials. In addition, the procedure described does not imply an unequivocal way for finding the errors
472 for the reversal potential estimates. Accordingly, for the synaptic input classification purposes, we varied
473 the reversal potentials in the predefined ranges when using Eqs. (6) and (7) to calculate the synaptic
474 conductances. We used the following ranges: [-20, 0] mV and [-110, -90] mV for the reversal potentials
475 for excitation and inhibition, respectively. ***Figure 6*** illustrates that although the absolute values of the
476 conductances vary to some extent as we vary the reversal potentials, the shape of their reconstructed
477 profiles remains consistent.

478

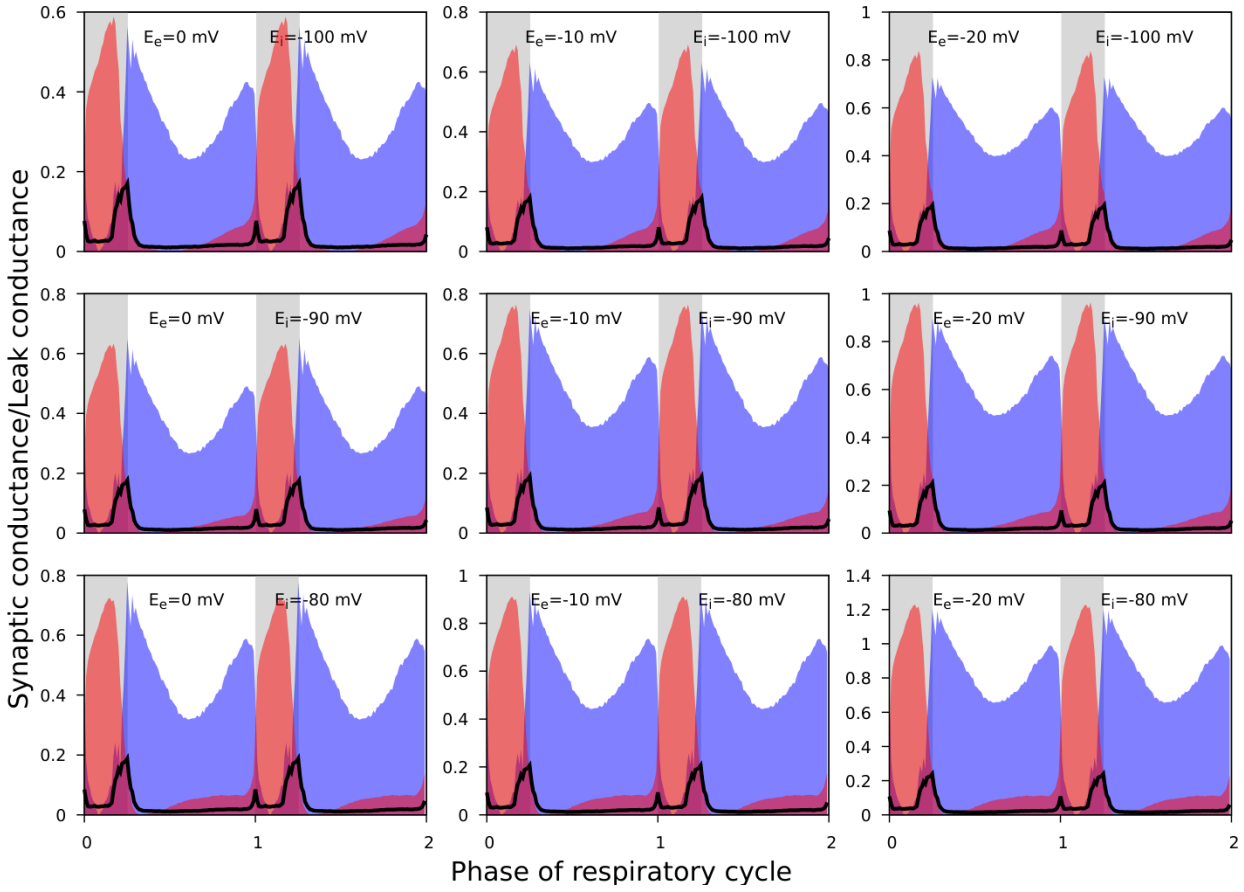

479

480 **Figure 6. The effect of reversal potential variation on the synaptic input reconstruction results.** We
481 used the recording of the ramp-I neuron shown in Fig. 3B5 and recalculated its synaptic conductances for
482 different combinations of the inhibitory and excitatory reversal potential values as indicated in each plot.
483 Synaptic conductances are normalized by the estimates of the leak conductance. While the absolute

conductance values vary with the reversal potentials, the shapes of the synaptic profiles as well as the relationship between the excitatory and inhibitory conductances are consistent across different values of the excitatory and inhibitory reversal potentials used.

Evaluating the effects of non-stationarity of the intracellular recordings. Our approach implicitly assumes that the intrinsic properties of the recorded neurons do not change (much) throughout the epoch used for the calculations. To verify the plausibility of this hypothesis, whenever possible we used two different epochs from the same recordings satisfying the criteria formulated in the *Preprocessing* section of the Methods for the complete analysis. We found that differences between the results for different epochs in most cases were comparable to those observed in the recordings obtained by current- and voltage-clamp protocols from the same neuron. ***Figure 7*** shows the results for two adjacent non-overlapping epochs for three different neurons.

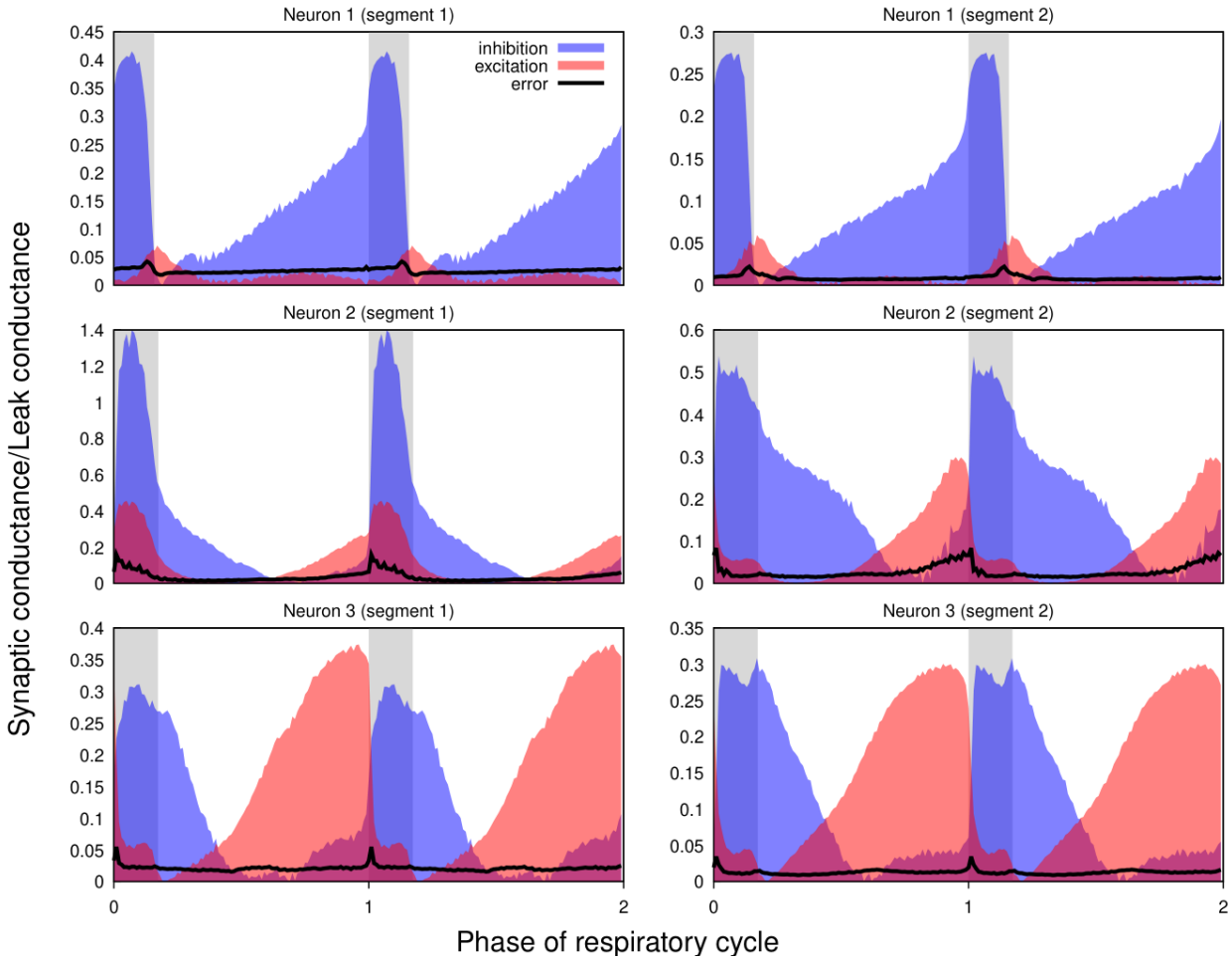

Figure 7. Non-stationarity of the recordings does not qualitatively affect the reconstructed profiles of

synaptic conductances. Synaptic conductance profiles calculated using non-overlapping segments of the recordings (left and right) from three different neurons (post-I, top; aug-E, middle and bottom). The similarities of the conductance profiles for different segments reflect the stability of the recordings and neuronal intrinsic properties and patterns of synaptic inputs.

In summary, our evaluation of the major assumptions and potential sources of error with our procedures for extracting temporal patterns of synaptic conductances, including recording procedures, and cycle phase-dependent linearity of current-voltage relations (***Figure 1 Supplemental Figure 1***), indicate that the temporal profiles of conductances obtained by our method are reliable for functional circuit reconstruction as we elaborate further below.

Discussion

In our analyses of synaptic conductance profiles in rhythmically active neurons from neuronal intracellular recordings, we propose that these profiles represent the convergent synaptic inputs from many neurons, and therefore represent the synaptic interactions of key functional populations operating in the active networks, which provides a basis for functional network reconstruction. Accordingly, a main objective of this study was to establish the utility and reliability of our technique, based on theoretical analyses and experimental validation, for extracting and separating profiles of inhibitory and excitatory conductances at high temporal resolution from intracellular recording data. We demonstrate the efficiency and robustness of our technique by applying our analyses to infer synaptic inputs to rhythmically active respiratory neurons comprising key microcircuits within the medullary preBötC and BötC regions of the brainstem respiratory CPG, which provided a diversity of neuronal electrophysiological phenotypes in various rhythmic microcircuits to test the performance of our technique. Our approach extends previously proposed methods for extracting dynamic patterns of synaptic conductances in post-synaptic neurons in various other neural circuits (Borg-Graham *et al.*, 1998; Anderson *et al.*, 2000; Shu *et al.*, 2003; Berg *et al.*, 2007; Endo & Kiehn, 2008; Wright & Calabrese, 2011), by providing higher temporal resolution with nearly continuous readouts of inhibitory and excitatory synaptic conductances, in our illustration throughout the respiratory cycle for different respiratory interneuron types. We have obtained previously unavailable synaptic conductance profiles for the different neuron populations, and illustrate how this analysis can be used to infer functional

528 interactions and circuit configurations of interneuron populations, which demonstrates the utility of our
529 technique. Below we further address technical issues affecting the robustness of our approach, and then
530 discuss the general applicability to rhythmically active circuits.

531 **Estimation of reversal potentials and errors in conductance analysis**

532 We have noted above and evaluated uncertainties concerned with synaptic reversal potentials and
533 assumptions about stability of the cellular properties and recordings on the inferred synaptic
534 conductance profiles, but it is important to elaborate certain points. We have used an experimental
535 preparation and setup that provides optimal stability for sharp electrode intracellular recordings. We
536 used strict criteria for assessing and accepting the quality and stability of the recordings. For the most
537 part, our analysis results for a given neuron that meets our criteria were reproducible for different
538 recording epochs and conditions. We also generated continuous error estimates for each example shown
539 and confirmed the statistical significance of conductance values. Regarding stationarity, our results
540 suggest that any differences between the inferred conductance profiles for different recording epochs
541 and conditions in most cases were comparable to those between recordings obtained by current- and
542 voltage-clamp protocols.

543 Most neurons that we have analyzed receive inhibition only during certain parts of respiratory
544 cycle regardless of whether they are inspiratory or expiratory neuron types. This allowed retrieving their
545 reversal potentials for inhibition using the approach described in Materials and methods. Interestingly,
546 the inhibitory synaptic reversal potentials retrieved turned out to vary significantly among cells between
547 -62 mv and -116 mV. The reversal potential estimates were in good correspondence with actual reversals
548 of inhibitory events when a cell was hyperpolarized below the reversal potential. Therefore, regarding
549 the analysis, the results were reliable. Nevertheless, on average, reversal potentials were much more
550 negative than what would have been expected. It is well known that in intracellular recordings, the
551 length constant of the neuron and the distance of the microelectrode from the synaptic inputs
552 determine the measured reversal potential (Calvin, 1969; Spruston *et al.*, 1993; Wehr & Zador, 2003). For
553 the precise extraction of inhibitory and excitatory conductances from the total conductance, reversal
554 potential values may be critical. The variability of the inhibitory reversal potential emphasizes the need
555 to determine the reversal potential for each neuron separately. Otherwise, a wrong inhibitory reversible
556 potential value used for the reconstruction may lead to incorrect conductance profiles. For example, a
557 large positive bias in the inhibitory reversal potential will have the effect that a part of the inhibitory
558 conductance may be mislabeled as excitatory conductance and therefore show a pattern of concurrent

559 inhibition and excitation. Our method for the estimation of inhibitory reversible potential appeared very
560 reliable when compared to the experimental estimates of the inhibitory reversal potential and
561 essentially excluded the occurrence of this excitatory conductance artifact.

562 The absolute values of inhibitory and excitatory conductance calculated by the analysis are
563 contaminated with an error depending on the length constant of the neuron and the distance of the
564 microelectrode from the synaptic inputs (Calvin, 1969; Wehr & Zador, 2003). Importantly, Wehr and
565 Zador (2003) show that the estimate of timing of synaptic conductances is reliable and not influenced by
566 the length constant of the neuron. Therefore, the conductance profiles extracted with our analysis are
567 qualitatively reliable and the overall time course of inhibitory and excitatory conductances reflect the
568 overall inhibitory and excitatory inputs to the different electrophysiological classes of active neurons
569 analyzed.

570 **Implications of reconstructed synaptic conductance profiles for respiratory functional circuit**
571 **architecture**

572 Our analysis revealed different sets of inhibitory and excitatory synaptic conductances that are
573 characteristic for the different populations of respiratory neurons. Indeed, our results suggest that phasic
574 excitatory and inhibitory synaptic inputs that result from network interactions of these respiratory
575 neuron populations shape membrane potential trajectories and spiking patterns of the neurons
576 throughout the respiratory cycle. What can we learn from these results about the organization and
577 operation of the underlying pattern generation networks?

578 We have suggested circuit motifs that are consistent with the patterns of synaptic inputs to the
579 various neurons, and which also account for our immuno-histochemical identification of inhibitory
580 neurons as subpopulations of most of the electrophysiological types. However, these circuit elements do
581 not explain the overall dynamical operation of the circuits, particularly how the rhythm and the orderly
582 generation of the multiple activity phases occurs. A more comprehensive synthesis of circuit interactions
583 as illustrated below, and ultimately computational simulation studies (e.g., (Lindsey et al., 2012; Molkov
584 et al., 2017), are required. In ***Figure 4 Supplemental Figure 1*** we illustrate the construction of a
585 combinatorial circuit schematic of the functional connectivity from the neuronal population interactions
586 suggested by our collection of circuit motifs.

587 Previously, computational models for core circuits of the respiratory CPG including interacting
588 microcircuits in the preBötC and BötC regions have proposed a network organization with respiratory

neuron population interactions that are capable from simulation studies with models incorporating circuit architectures (e.g., ***Figure 4 Supplemental Figure 1B***) and neuronal and synaptic biophysical properties to generate a realistic respiratory rhythm and the three-phase rhythmic pattern of neuron and neuronal population activity (Lindsey et al., 2012; Molkov et al., 2017; Rubin, Shevtsova, Ermentrout, Smith, & Rybak, 2009; Rybak et al., 2007). These include the model proposed by Smith, Abdala, Koizumi, Rybak, and Paton (2007) based on regional circuit mapping and electrophysiological studies with the mature rat *in situ* experimental preparation used in the present studies. Despite its plausibility, this and other models remain speculative because the experimental evidence for functional connectivity is mostly indirect.

Our cellular-based analysis provides a way of untangling functional connections within the respiratory CPG and testing computational models. By assuming the origin of these inputs according to the phase in which they occur, we can draw conclusions on the functional connections between the key respiratory neuron populations recorded here. Our synaptic conductance profiles are consistent with multiple features of the network architecture and interactions proposed by Smith et al. (2007) as illustrated in ***Figure 4 Supplemental Figure 1B***, which was suggested to be a minimal and sufficient circuit configuration to explain how the three-phase rhythmic respiratory pattern, including activity patterns of key interneuron populations in the medulla, can be generated. As reconstructed from our synaptic conductance profiles and collection of circuit motifs, there are new features in our more elaborate circuit connectome in the new combinatorial circuit schematic in ***Figure 4 Supplemental Figure 1A*** as noted in the supplemental figure legend. There are likely additional connectivity features that remain to be uncovered as the catalogue of intracellular recording data and inferred functional interactions is expanded from further studies. We note that the profiles of neuronal synaptic interactions that we consider are specific for the *in situ* reduced rat brainstem-spinal cord system, which has proven to be an important model system for understanding the operation of core CPG respiratory circuits in the medulla and pontine reticular formation that are operational in our experimental set-up (Paton *et al.*, 2022), but cannot account for the supra-brainstem and peripheral circuit inputs in the nervous system *in vivo* (e.g., Lindsey *et al.*, 2012; Smith *et al.*, 2013; Paton *et al.*, 2022). Our objective here was to illustrate how our techniques can delineate the functional circuit interactions in an established core set of circuits in the respiratory CPG as an example of the utility of our approach that can be generally applied to rhythmic neural circuits as discussed below.

620 **Applicability to other rhythmically active networks**

621 Our method for extracting and separating phasic patterns of inhibitory and excitatory synaptic
622 conductances from single neuronal intracellular recordings is broadly applicable to rhythmic circuits
623 which are ubiquitous in nervous systems. Our approach involves phase-based analysis, where the
624 network activity cycle is divided into activity phases to capture dynamic changes of synaptic input
625 conductances throughout the activity cycle. This approach is relevant for any circuits with repetitive
626 activity cycles, such as rhythmic CPG motor networks (e.g., (Calabrese & Marder, 2024)) and circuits
627 generating cortical rhythms (Yuste *et al.*, 2005). The method is based on the general mathematical
628 framework presented, involving current balance equations and linear regression to separate excitatory
629 and inhibitory conductances, and therefore is applicable to different rhythmic neuron types and circuits
630 and is suitable for diverse experimental setups. By providing high-resolution temporal profiles of synaptic
631 inputs and outputs (below, based on neuronal spiking patterns), this method enables researchers to infer
632 the functional connectivity and dynamic interactions within any rhythmically active network.

633 Applying this method, as we have illustrated for respiratory circuits, to other rhythmic networks
634 such as locomotor or cortical circuits including sensory processing networks, follows a similar process for
635 extracting neuronal excitatory and inhibitory inputs during different oscillatory phases of endogenous or
636 sensory-driven periodic activity. This allows for the inference of functional synaptic input connections for
637 any targeted neuron populations based on the timing and strength of the extracted synaptic inputs. In
638 this context, functional populations are defined as groups of neurons with similar firing patterns with
639 respect to the cycle phase. If the synaptic conductance profile of a recorded neuron contains a
640 component that mirrors the firing pattern of a specific population, it can be inferred that there is a
641 functional connection from that population to the recorded neuron. Similarly, in sensory processing
642 networks, it can reveal how sensory inputs are synaptically integrated in neurons by examining synaptic
643 conductance patterns in response, for example, to repetitive stimuli.

644 The approach that we have described is versatile since it is compatible with various recording
645 protocols, such as current-clamp and voltage-clamp and different modes of intracellular recording (sharp
646 electrode or whole-cell patch clamp). We note that our approach to defining functional connectivity
647 does not provide information on locations of the sources of the synaptic inputs, although we can infer
648 spiking patterns of the source neurons from the temporal features of the synaptic conductance profiles.
649 These profiles represent the total synaptic inputs that can arise from many neurons possibly with short
650 and long-range axonal projections to a given neuron. The capability of our approach to readout the total

synaptic conductance and separate the excitatory and inhibitory components from all sources at high temporal resolution is a strength of our approach. These inferred neuronal population connections from the electrophysiological analyses provided by our technique can be further mapped and corroborated with other functional and anatomical approaches.

In summary, the versatility of our technique lies in its foundation on basic electrophysiological principles and adaptability to different rhythmic activities making it a powerful tool for investigating a wide range of rhythmically active neuronal networks and potentially offering insights into their functional organization and dynamic operations.

Materials and methods

Animal procedures

All animal procedures were approved by the Animal Care and Use Committee of the National Institute of Neurological Disorders and Stroke (Animal Study Proposal #1154-21).

In situ perfused rat brain-stem spinal cord preparation

Experiments were performed using the *in situ* arterially perfused brainstem-spinal cord preparations from mature (3–4 weeks old) rats (Paton, 1996; Paton *et al.*, 2022) following experimental procedures described in detail in Smith *et al*. 2007 and modified as described below to provide optimal conditions for intracellular recording. Briefly, preheparinzed (1,000 units, given intraperitoneally) rats (Sprague-Dawley, 45-70g; male) were anaesthetized deeply with 5% isoflurane and the portion of the body caudal to the diaphragm was removed. The head and thorax were immersed in ice-chilled carbogenated Ringer solution and the brain was decerebrated at a precollicular level. The descending aorta, phrenic nerve, central vagus and hypoglossal nerves were surgically isolated. The dorsal brainstem was exposed by craniotomy and cerebellectomy. To achieve the mechanical stability necessary for intracellular recordings, the great veins and heart were removed. The preparation was transferred to a recording chamber and the descending aorta cannulated with a double lumen catheter for perfusion and recording of perfusion pressure with a pressure transducer. A hydraulic damping Windkessel chamber was used in the perfusion circuit immediately downstream from the output of the roller pump (Watson-Marlow, Wilmington, MA) to eliminate peristaltic flow pulsations that affect stability of the sharp electrode intracellular recordings.

680

681 ***Solutions and pharmacological agents***

682 The perfusate contained the following in distilled water: magnesium sulphate (MgSO4 -1.25 mM),
683 potassium phosphate (KH_2PO_4 - 1.25 mM), potassium chloride (KCl - 5.0 mM), sodium bicarbonate
684 ($NaHCO_3$ - 25 mM), sodium chloride (NaCl -125 mM), calcium chloride ($CaCl_2$ - 2.5 mM), dextrose (10
685 mM) and polyethylene glycol (0.1785 mM). Vecuronium bromide was added to the perfusate to block
686 neuromuscular transmission (4 µg/ml; SUN pharmaceutical industries, Bryan, USA). The perfusate was
687 gassed with 95%O2-5%CO2 and maintained at 31°C. Vasopressin (200–400 pM as required; APP
688 pharmaceuticals, East Schaumburg, USA) was added to the perfusate to raise and maintain perfusion
689 pressure at 70–80 mmHg. Unless stated, all chemicals were from Sigma.

690

691 ***Electrophysiological recordings and neuron labeling***

692 Efferent activity of the phrenic (PN) and central vagus (VN) nerves were recorded simultaneously with
693 glass suction electrodes and their activities were amplified, filtered (0.3–6.0 KHz), rectified and
694 integrated (50 ms time constant). Sharp microelectrode somatic intracellular recordings were made in
695 the preBötC and BötC regions. The brainstem was mapped by recording population activity of neurons in
696 the medulla oblongata with an extracellular electrode (5–10 MOhm) prior to intracellular recording. The
697 position of the electrode was monitored by software that kept track of the micromanipulator mechanical
698 coordinates. Once the region of the preBötC or BötC was identified by rhythmic inspiratory/expiratory
699 population activity, coordinates were saved and in some cases the brainstem surface was marked with
700 pontamine sky blue dye. Intracellular recordings were made with fine tipped glass microelectrodes (45 to
701 70 MOhm) pulled from borosilicate glass capillaries. The microelectrodes for intracellular recording were
702 driven into the recording site by a combination DC motor driven micromanipulator with an integrated
703 piezotranslator (PM10-1, Marzhauser Wetzlar, Germany), allowing high stepping speeds for cell
704 penetration. A dual current clamp-voltage clamp amplifier (SEC-05X, NPI, Tamm, Germany) was used to
705 amplify the signals in bridge and discontinuous current clamp (DCC) recording modes. Discontinuous
706 single electrode voltage clamp (SEVC) recordings were obtained by exploiting the high switching
707 frequencies and electrode capacity compensation of the SEC-05X system, allowing high fidelity SEVC
708 recordings with the high resistance sharp microelectrodes used. The microelectrodes were filled with a
709 solution of 2 M potassium acetate (KAc) and 0.1 M potassium chloride (KCl) and 4% neurobiotin. During

710 recordings some neurons were labeled by ionophoresis of neurobiotin into the cell. All recordings were
711 digitized via a CED 1401-plus multi-channel interface and acquired (6–12 kHz digitization rates) using CED
712 Spike 2 software.

713

714 ***Histological analysis***

715 Transected brain stem was fixed in 4% buffered (0.1 M phosphate buffer) paraformaldehyde for 24 h at
716 4°C, cryoprotected at 4°C in 30% sucrose, and subsequently coronally sectioned (30 µm thick) on a
717 freezing microtome. All the floating sections were preincubated for 1 h with 10% donkey serum in PBS
718 and subsequently incubated for 48-72h at room temperature with primary antibodies: Rabbit anti-
719 Glycine antibody (1:5000; Immunosolution), rabbit anti-GABA antibody (1:1000; Millipore-Sigma), and
720 goat anti-ChAT antibody (1:500; Chemicon). Labeling for neuronal ChAT expression was used to label
721 motoneurons of nucleus ambiguous to verify the region where the neurons were recorded and to
722 confirm that the recordings were obtained from non-motoneurons. Floating sections were incubated for
723 2 h at room temperature with a mixture of donkey anti-rabbit IgG conjugated with Cy5 and donkey anti-
724 goat IgG conjugated with Cy3 (1:500; Jackson ImmunoResearch). For fluorescence labeling of neurons
725 filled with neurobiotin during electrophysiological recording, slices were incubated with Alexa Fluor 488-
726 Avidin D (1:500, Invitrogen). Tissue was mounted on slides and covered with antifading medium.
727 Confocal images were obtained with a laser-scanning microscope (LSM 510 Meta, Zeiss). Alexa Fluor 488,
728 Cy3, and Texas Red or Cy5 were detected at 488, 543, and 633 nm emission wavelengths, respectively.
729 Images were acquired and processed with a Zeiss Zen software and presented as single optical sections
730 selected from serial optical sections (Z-stacks).

731

732 ***Reconstruction of synaptic inputs from intracellular recordings***

733 <u>Preprocessing</u>

734 Inhibitory and excitatory synaptic inputs to respiratory neurons were reconstructed from intracellular
735 recordings using a general approach similar to that described by Berg *et al.* (2007) and others (Borg-
736 Graham *et al.*, 1998; Anderson *et al.*, 2000; Shu *et al.*, 2003; Endo & Kiehn, 2008).

737 During intracellular recordings for conductance measurement and subsequent decomposition of
738 inhibitory and excitatory inputs, depolarizing and hyperpolarizing current was injected into the cell in a

stepwise manner (***Figure 1A***). The period of time from the onset of the phrenic burst to the beginning of the next phrenic burst was used as reference cycle. The beginning of a phrenic burst was determined as 10% of phrenic amplitude in the rectified and low pass filtered (time constant = 0.05s) extracellular recording. We only analyzed recordings from respiratory neurons that fulfilled the following criteria: (1) The coefficient of variation of the respiratory cycle period was <10%; (2) At least three steps of current injections were made during intracellular recording that were kept constant for at least 5 respiratory cycles each. Neurons with obvious recording instability such as significant changes in membrane leakage current with a baseline membrane potential drift were not analyzed. The intracellularly recorded membrane potential $V_m(t)$ was sampled down from 12.5 kHz to 100 Hz. To eliminate spikes without affecting slow membrane potential fluctuations the voltage trace $V_m(t)$ was processed using median filtration.

<u>Error estimation</u>

After performing linear regression (2) for each phase bin we have standard errors $\delta R(\varphi)$ and $\delta V_0(\varphi)$ of the total resistance $R(\varphi)$ and the resting potential $V_0(\varphi)$ respectively which are defined by voltage fluctuations and by the number of respiratory cycles in the epoch used for reconstruction. Based on this we can approximately calculate the standard error for the total conductance $\delta G(\varphi) = \delta R(\varphi)/R^2(\varphi)$, which can be used as an overestimate for the errors of both excitatory and inhibitory conductances since the total conductance is a sum of the two. Calculation of the dynamic components involves subtraction of the minimal values of the calculated synaptic conductances. Therefore, the dynamic components' standard errors can be estimated as $\delta\Delta G_{i,e}(\varphi) = \sqrt{\delta G(\varphi)^2 + \delta G(\varphi_m)^2}$, where φ_m is the phase where the corresponding conductance (excitatory or inhibitory) attains its minimum.

<u>Statistical significance</u>

Considering the relatively large sample sizes (for each cell analyzed we had 50-200 respiratory cycles long recordings), we used a one-tailed z-test to confirm statistical significance of the reconstructed synaptic inputs by testing a null hypothesis that the dynamical component of the synaptic conductance is zero (no different from its minimal value). Specifically, at each phase of the respiratory cycle φ for the dynamic components of inhibitory and excitatory conductances we calculated their z-scores $Z_{i,e}(\varphi) =$

$\Delta G_{i,e}(\varphi)/\delta\Delta G_{i,e}(\varphi)$, and corresponding p-values. We used p-value < 0.05 criterion to accept the alternative hypothesis that the calculated dynamic component of the synaptic conductance at a particular phase is statistically significantly greater than zero. In the latter case, we concluded that the recorded cell received the corresponding type of synaptic input (excitatory or inhibitory) during the corresponding part of the respiratory cycle (inspiration, post-inspiration, or late-expiration/pre-inspiration).

Acknowledgements

This study was supported by NIH grants R01 NS057815, R01 NS069220, R01 AT008632, Alexander von Humboldt Foundation, and the Intramural Research Program of the NIH, NINDS.

References

Anderson JS, Carandini M & Ferster D. (2000). Orientation tuning of input conductance, excitation, and inhibition in cat primary visual cortex. *J Neurophysiol* **84,** 909-926.

Ausborn J, Koizumi H, Barnett WH, John TT, Zhang R, Molkov YI, Smith JC & Rybak IA. (2018). Organization of the core respiratory network: Insights from optogenetic and modeling studies. *PLoS Comput Biol* **14,** e1006148.

Berg RW, Alaburda A & Hounsgaard J. (2007). Balanced inhibition and excitation drive spike activity in spinal half-centers. *Science* **315,** 390-393.

Bianchi AL, Denavitsaubie M & Champagnat J. (1995). Central Control of Breathing in Mammals - Neuronal Circuitry, Membrane-Properties, and Neurotransmitters. *Physiological Reviews* **75,** 1-45.

Borg-Graham LJ, Monier C & Fregnac Y. (1998). Visual input evokes transient and strong shunting inhibition in visual cortical neurons. *Nature* **393,** 369-373.

Buzsáki G. (2006). *Rhythms of the brain*. Oxford University Press, Oxford ; New York.

Calabrese RL & Marder E. (2024). Degenerate Neuronal and Circuit Mechanisms Important for Generating Rhythmic Motor Patterns. *Physiological Reviews***,** (in press).

Calvin WH. (1969). Dendritic synapses and reversal potentials: theoretical implications of the view from the soma. *Exp Neurol* **24,** 248-264.

Cohen MI. (1979). Neurogenesis of respiratory rhythm in the mammal. *Physiol Rev* **59,** 1105-1173.

Endo T & Kiehn O. (2008). Asymmetric operation of the locomotor central pattern generator in the neonatal mouse spinal cord. *J Neurophysiol* **100,** 3043-3054.

Ezure K, Tanaka I & Kondo M. (2003). Glycine is used as a transmitter by decrementing expiratory neurons of the ventrolateral medulla in the rat. *The Journal of neuroscience : the official journal of the Society for Neuroscience* **23,** 8941-8948.

Feldman JL & Smith JC. (1995). Neural Control of Respiratory Pattern in Mammals: An Overview. In *Regulation of breathing*, 2nd edn, ed. Dempsey JA & Pack AI, pp. 39-69. M. Dekker, New York.

Koizumi H & Smith JC. (2008). Persistent Na+ and K+-dominated leak currents contribute to respiratory rhythm generation in the pre-Botzinger complex in vitro. *J Neurosci* **28,** 1773-1785.

Lindsey BG, Rybak IA & Smith JC. (2012). Computational models and emergent properties of respiratory neural networks. *Compr Physiol* **2,** 1619-1670.

Molkov YI, Rubin JE, Rybak IA & Smith JC. (2017). Computational models of the neural control of breathing. *Wiley Interdiscip Rev Syst Biol Med* **9**.

Paton JF. (1996). A working heart-brainstem preparation of the mouse. *J Neurosci Methods* **65,** 63-68.

Paton JFR, Machado BH, Moraes DJA, Zoccal DB, Abdala AP, Smith JC, Antunes VR, Murphy D, Dutschmann M, Dhingra RR, McAllen R, Pickering AE, Wilson RJA, Day TA, Barioni NO, Allen AM, Menuet C, Donnelly J, Felippe I & St-John WM. (2022). Advancing respiratory-cardiovascular physiology with the working heart-brainstem preparation over 25 years. *J Physiol* **600,** 2049-2075.

Richter DW. (1996). Neural regulation of respiration: rhythmogenesis and afferent control. In *Comprehensive Human Physiology*, ed. Greger R & Windhorst U, pp. 2079-2095. Springer-Verlag, Berlin.

Richter DW & Smith JC. (2014). Respiratory rhythm generation in vivo. *Physiology (Bethesda)* **29,** 58-71.

Richter DW & Spyer KM. (2001). Studying rhythmogenesis of breathing: comparison of in vivo and in vitro models. *Trends Neurosci* **24,** 464-472.

Shu Y, Hasenstaub A & McCormick DA. (2003). Turning on and off recurrent balanced cortical activity. *Nature* **423,** 288-293.

Smith JC, Abdala AP, Borgmann A, Rybak IA & Paton JF. (2013). Brainstem respiratory networks: building blocks and microcircuits. *Trends Neurosci* **36,** 152-162.

Spruston N, Jaffe DB, Williams SH & Johnston D. (1993). Voltage- and space-clamp errors associated with the measurement of electrotonically remote synaptic events. *J Neurophysiol* **70,** 781-802.

Wehr M & Zador AM. (2003). Balanced inhibition underlies tuning and sharpens spike timing in auditory cortex. *Nature* **426,** 442-446.

Wright TM, Jr. & Calabrese RL. (2011). Patterns of presynaptic activity and synaptic strength interact to produce motor output. *J Neurosci* **31,** 17555-17571.

Yuste R, MacLean JN, Smith J & Lansner A. (2005). The cortex as a central pattern generator. *Nat Rev Neurosci* **6,** 477-483.